#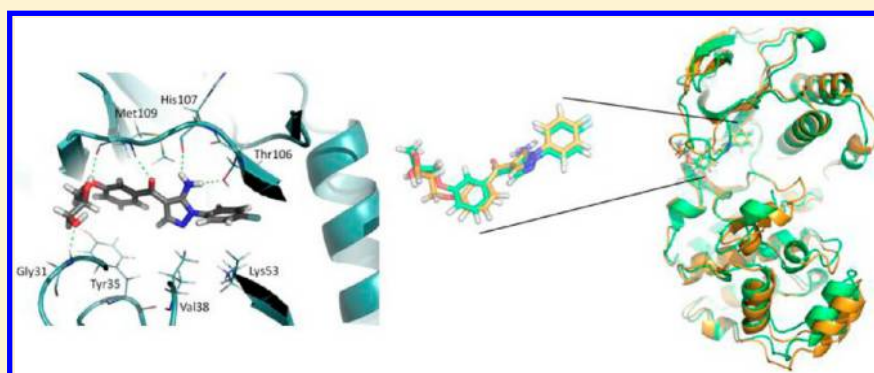 Molecular Modeling of p38α Mitogen-Activated Protein Kinase Inhibitors through 3D-QSAR and Molecular Dynamics Simulations

Hsin-Wen Chang,[†] Fu-Sheng Chung,[‡] and Chia-Ning Yang[†,‡,*]

[†]Institute of Biotechnology and [‡]Department of Life Science, National University of Kaohsiung, Taiwan

S Supporting Information

ABSTRACT: The p38 mitogen-activated protein kinase (MAPK) signaling pathway plays an essential role in inflammation and other physiological processes. Because specific inhibitors of p38α and p38β MAPK block the production of the major inflammatory cytokines and other proteins, p38α and p38β MAPK represent promising targets for the treatment of inflammation. In this work, a series of p38α inhibitors based on the structural scaffold of 4-benzoyl-5-aminopyrazole were analyzed using a combination of molecular modeling techniques. We generated three-dimensional quantitative structure-activity relationship (3D-QSAR) models for both comparative molecular field analysis (CoMFA) and comparative molecular similarity index analysis (CoMSIA) to highlight the structural requirements for p38 MAPK inhibition. Furthermore, we employed molecular dynamics (MD) simulations and the MM/GBSA method to compare the binding modes and binding free energies of a potent and selective compound interacting with p38α, p38β, p38γ, and p38δ MAPK in detail. Contour maps generated via 3D-QSAR analysis identified several key interactions that were also indicated through MD simulations. The binding free energies calculated via the MM/GBSA method were strongly correlated with experimentally observed biological activities and explained the selective inhibition of p38α and p38β, but not p38γ and p38δ detected here. On the basis of the obtained results, we provide insights regarding the development of novel potent p38α MAPK inhibitors.

INTRODUCTION

The p38 mammalian mitogen-activated protein kinase (MAPK), also referred to as cytokine-suppressive anti-inflammatory drug-binding protein (CSBP), is the mammalian ortholog of the yeast HOG kinase, which was first discovered in 1994.[1] p38 MAPK belongs to a family of proline-directed serine/threonine kinases comprised of four p38 MAPK isoforms: p38α (MAPK14), β (MAPK11), γ (Erk6 or MAPK12), and δ (MAPK13 and SAPK4). The p38 MAPK isoforms share 40−60% structural homology with each other.[2−4] However, the functions of p38β, p38γ, and p38δ have not yet been identified. p38 MAPK is involved in regulating HSP27, MK2 (MAPKAPK-2), MK3 (MAPKAPK-3), and several transcription factors, including ATF-2, Stat1, the Max/Myc complex, MEF-2, and Elk-1, as well as indirectly regulating CREB through the activation of MSK1.[5−10] The p38 MAPK signaling cascade controls cellular responses to pro-inflammatory and stress stimuli, including osmotic shock, inflammatory cytokines, lipopolysaccharide (LPS), UV light, and growth factors that regulate various cellular processes, such as inflammation, the cell cycle, apoptosis, development, cell differentiation, senescence, and tumorigenesis.[10−15]
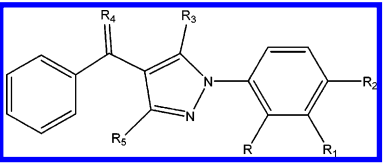
A growing body of recent literature has described the role of p38 MAPK in a variety of diseases. p38 MAPK activation is critical in inflammatory and autoimmune diseases such as rheumatoid arthritis,[16] osteoporosis, Crohn's disease,[17] inflammatory bowel disease, asthma,[18] toxic-shock syndrome, and psoriasis. Recent studies have also highlighted the broad effect of p38 MAPK activation in regulating other aspects of cell physiology, such as controlling the cell cycle and cytoskeleton remodeling, which are associated with cancer-related cellular responses.[11,12] Thus, the p38 MAPK pathway displays important pathological functions and serves as a potential therapeutic target for treating human diseases.

Recent studies have advanced the understanding of p38 MAPK regulation and its in vivo function. The use of kinase inhibitors in genetically modified mouse cells lacking various p38 MAPK signaling cascade components provides important information regarding the physiological roles of p38 MAPK, the mechanisms involved in p38 MAPK signal transduction, and

Table 1. Chemical Structures and IC$_{50}$ Values of the 39 Compounds Used to Develop the QSAR Models[a]

Compd. No.	Substituent						IC$_{50}$ (µM)
	R	R$_1$	R$_2$	R$_3$	R$_4$	R$_5$	
1*	H	H	H	NH$_2$	O	H	2.30
2	H	H	H	CN	O	H	1,000
3	H	H	H	OH	O	CH$_3$	1,000
4*	CH$_3$	H	H	NH$_2$	O	H	1.08
5*	H	NO$_2$	H	NH$_2$	O	H	64.2
6	H	H	F	NH$_2$	O	H	1.10
7	H	F	H	NH$_2$	O	H	6.7
8	F	H	H	NH$_2$	O	H	2.86
9	H	H	OCH$_3$	NH$_2$	O	H	7.06
10*	OCH$_3$	H	H	NH$_2$	O	H	8.38
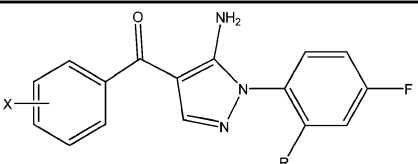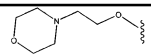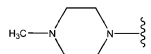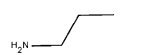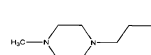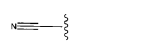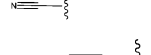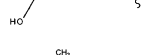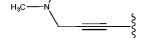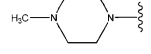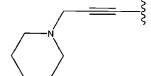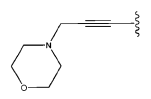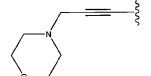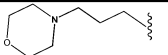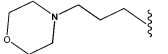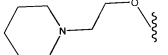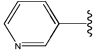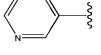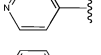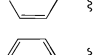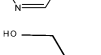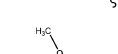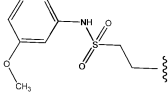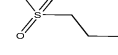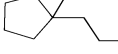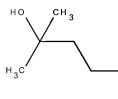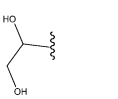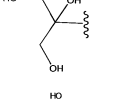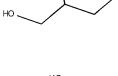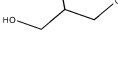
Compd. No.	Substituent		IC$_{50}$ (µM)
	X	R	
11	3-(2-morpholin-4-ylethoxy)	H	1.27
12	4-methylpiperazin-1-yl	H	2.00
13	2-aminoethyl	H	2.44
14	2-(4-methylpiperazin-1-yl)ethyl	H	1.64
15	3-cyano	H	4.76
16*	4-cyano	H	8.38
17	3-(3-hydroxyprop-1-ynyl)	H	4.04
18	3-dimethylaminoprop-1-ynyl	H	2.28
19	3-(4-methylpiperazin-1-yl)	H	2.65
20	3-piperidin-1-ylprop-1-ynyl	H	1.32
21	3-(3-morpholin-4-ylprop-1-ynyl)	H	1.72
22	4-(3-morpholin-4-ylprop-1-ynyl)	H	3.13

Table 1. continued

Compd. No.	Substituent		R	IC$_{50}$ (μM)
	X			
23*	3-(3-morpholin-4-ylpropyl)		H	1.74
24	4-(3-morpholin-4-ylpropyl)		H	22.3
25	2-piperidin-1-ylethoxy		H	1.84
26	3-pyridin-3-yl		H	0.78
27	4-pyridin-3-yl		H	0.98
28*	3-pyridin-4-yl		H	1.28
29	3-pyridin-4-yl		F	0.31
30	3-pyridin-3-yl		F	0.18
31	3-(2-hydroxyethyl)		H	0.85
32	3-(2-ethanesulfonic acid amide)		H	1.25
33	3-(2-methanesulfonylethyl)		H	0.79
34*	3-(2-(1-hydroxycyclopentyl)ethyl)		H	0.23
35	3-(3-hydroxy-3-methylbutyl)		H	0.59
36*	3-(1,2-dihydroxyethyl)		H	3.50
37	3-(1,2-dihydroxy-1-hydroxymethylethyl)		H	9.54
38	3-(2,3-dihydroxypropoxy) (R-form)		H	1.20
39	3-(2,3-dihydroxypropoxy) (S-form)		H	0.70

[a]Compounds indicated with * are in the test set.

p38 MAPK-mediated gene regulation in human diseases. Therefore, by examining the interaction of p38 MAPK with its inhibitors, information that will be useful for the development of novel, potent inhibitors can be obtained.

Studies have identified numerous structurally diverse inhibitors of p38α MAPK targeting the ATP-binding site, such as the pyridinyl imidazole mainframe SB203580, the pyrimidopryidazinone scaffold VX745, the pyrazole ketone RO3201195, the

indole amide SCI0469, and the pyrimidinone AMG548.[19] Goldstein et al. reported a novel class of highly selective p38α MAPK inhibitors with a 4-benzoyl-5-aminopyrazole scaffold. The lowest IC_{50} value for a member of this class of compounds was 0.18 μM (compound **30** in Table 1).[20] Moreover, among the reported compounds, compound **39** displayed in vitro selectivity against 105 kinases, yet only inhibited p38α, p38β, EPHA5, GAK, JNK2, JNK3, LCK, and PDGFRβ.[20]

Simulations based on molecular dynamics represent a powerful modern molecular modeling tool that enables scientists to understand molecular structures and dynamics in detail, particularly for examining the motion of individual atoms, which can be tracked over time. Accompanied by experimental observations, researchers have employed simulations of molecular dynamics (MD) to investigate protein-protein and protein-small compound interactions.[21−25] In addition, 3D structure-activity relationship (3D-QSAR) methods, including comparative molecular field analysis (CoMFA)[26] and comparative molecular similarity index analysis (CoMSIA),[27] make an auxiliary contribution to drug design through deriving structural information in interactive fields and predicting the influence on activity.

In the present study, a protocol combining the 3D-QSAR, MD, and MM/GBSA methods was applied to investigate the interactions of the p38α inhibitors synthesized by Goldstein et al. in detail. We conducted 3D-QSAR analysis to determine the structural requirements for the development of p38α MAPK inhibitors for use as drugs. MD simulations and binding free-energy calculations were performed using the MM/GBSA approach[28] for compound **39** bound to p38α and its three isoforms. Despite the fact that the isoforms of p38 share 40−60% structural homology, **39** is able to selectively discriminate among p38 isoforms, inhibiting p38α and p38β, but not p38γ and p38δ. Therefore, one goal of this study was to reveal the mechanism of **39**'s selectivity for the four p38 isoforms. The MD results obtained for p38α-**39** were in accord with the contour maps derived from 3D-QSAR and were compared to the three other complexes predicted by the MD simulations. In conclusion, by understanding the binding process of p38 inhibitors, we can obtain additional insights into potential structural modifications that may be generated to develop more potent and selective inhibitors of p38α MAPK.

COMPUTATIONAL METHODS

Setup for CoMFA and CoMSIA. The 39 investigated molecules and their p38α MAPK inhibitory activities were obtained from a data set designed, synthesized, and reported by Goldstein et al.[20] The molecular structures and IC_{50} values (μM) of the compounds in relation to p38α MAPK are listed in Table 1. We divided the 39 compounds into a training set of 30 compounds for model generation and a test set of 9 compounds (indicated by * in Table 1) for model validation. The test set compounds were selected based on the distribution of biological data and structural diversity (Figure 1 and Table 1). Compound **2** displays a reported IC_{50} value greater than 100 μM, whereas that for compound **3** is undetermined. After numerous trials, we set the IC_{50} values for these compounds to 1000 μM to extend the pIC_{50} to span values ranging from 3.00 to 6.74 and improve the statistical parameters when constructing 3D-QSAR models.

Compound alignment plays a critical role in determining structure−activity relationships because diverse inhibitory activities are strongly correlated with the substitution status on a given corner in a compound series. Because the studied compounds are all in the same core with minor modifications on R,
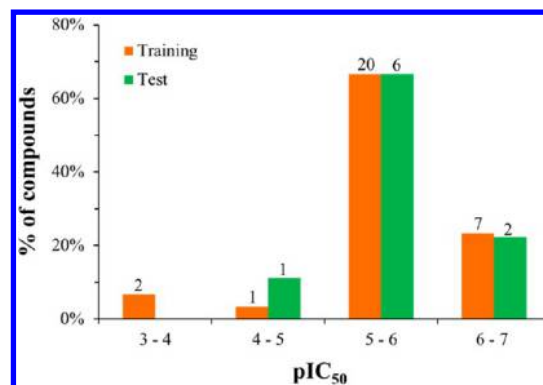
Figure 1. Distribution of the inhibitory activities of the training set and test set compounds in the 3D-QSAR analysis. The number above each bar specifies the compound number in the corresponding pIC_{50} range.

and $R_1 \sim R_5$ (see Table 1), we assumed that each compound bound to p38α MAPK would adopt a conformation similar to that of **39**. Therefore, all of the studied compounds were initially sketched based on the bound form of **39** within the p38α-**39** structure determined through X-ray crystallography. Using Gasteiger-Marsili charge assignment and Tripos force-field parameters, these structures were geometrically optimized through 500 steps by applying the Powell method without constraints. The database alignment protocol in Sybyl 8.1 was employed to align the structures according to the alignment core comprised of a benzoyl ring, pyrazole ring, and *N*-phenyl ring, as shown in Figure 2A. The alignment results are presented in
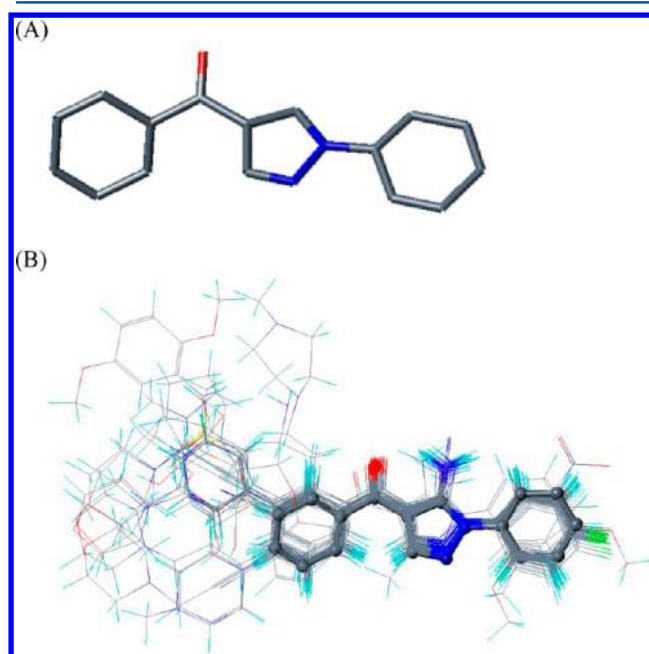
Figure 2. Alignment analysis. (A) Alignment core. (B) Alignment results for the 39 examined compounds from the training and test sets.

Figure 2B. To build the CoMFA model, we calculated two descriptors: steric (Lennard-Jones 6-12 potential) and electrostatic (Coulombic potential) field energies, using an sp^3 carbon atom carrying a +1.0 charge that served as a probe atom placed at the lattice point of a region box. For construction of the CoMSIA model, five similarity indices (steric, electrostatic, hydrophobic, H-bond donor, and H-bond acceptor) were calculated using a

probe atom with a 1 Å radius and a +1.0 charge. The 3D-QSAR models were built using the program Sybyl 8.1.[29] In partial least-squares (PLS) regression analysis, a leave-one-out (LOO) cross-validation was first performed to determine the optimal number of components (ONC). Furthermore, a noncross-validated analysis was conducted with the ONC to obtain the final QSAR model for CoMFA or CoMSIA.

Setup for Molecular Dynamics Simulations. The MD simulations were performed using the AMBER 11.0 software package[30] with the ff03.r1[31] and ff99SB force fields[32] to compare the selective binding modes of **39** to p38α, p38β, p38δ, and p38γ MAPK domains. The structure determined via X-ray crystallography (PDB code: 2GFS) was applied for the initial p38α-**39** complex and was superimposed upon p38β (in the DFG-out form), p38β (in the DFG-in form), p38δ, and p38γ to generate other **39**-bound complex structures. It is notable that in the retrieved structure, p38α is in the DFG-in form. The retrieved structures for p38β are reported in (i) the DFG-in form bound to compound B45365 (5-(2-chloro-4-fluorophenyl)-1-(2,6-di-chlorophenyl)-7-(1-propan-2-ylpiperidin-4-yl)-3,4-dihydroquinazolin-2-one) (PDB code: 3GC8) and (ii) the DFG-out form bound to compound nilotinib (4-methyl-*N*-[3-(4-methylimidazol-1-yl)-5-(trifluoromethyl)phenyl]-3-[[4-pyridin-3-ylpyrimidin-2-yl) amino]benzamide) (PDB code: 3GP0). The retrieved p38δ is reported in the DFG-in form (PDB code: 3COI), as is p38γ also in DFG-in form, which is bound to adenylyl imidodiphosphate ([[[[(2*R*,3*S*,4*R*,5*R*)-5-(6-aminopurin-9-yl)-3,4-dihydroxyoxolan-2-yl]methoxyhydroxyphosphoryl]-oxyhydroxyphosphoryl]amino]phosphonic acid) (PDB code: 1CM8). In all of the above cases, the bound compound was removed. In a recent study comparing numerous p38 MAP kinase inhibitors including those examined in this study, a preference for the DFG-in binding mode of the p38α inhibitors herein was reported.[33] Accordingly, our MD simulations for p38δ-**39** and p38γ-**39** based on the retrieved DFG-in active forms are considered relevant and appropriate. As carried out for p38β-**39**, we ran both DFG-in and DFG-out complexes for comparison. The force-field parameters for the ligand were generated with the general AMBER force field (GAFF) using the Antechamber program.[34] Partial atomic charges for the ligand atoms were assigned using the AM-BCC protocol[35] following the calculation of electrostatic potentials at the HF/6-31G* level. All of the hydrogen atoms in the four proteins were assigned using the LEaP module, which sets ionizable residues to their default protonation states at a neutral pH value. Each complex was immersed in a cubic box of TIP3P water molecules with a 12 Å minimum solute-wall distance.[36] A total of six, eight, seven, zero, and six Na⁺ ions were added to neutralize the p38α-, DFG-out p38β-, DFG-out p38β-, p38δ-, and p38γ-complex systems, respectively. Energy was minimized in the solvated system via progression through three stages, each employing 500 steps of the steepest descent algorithm and 500 steps of the conjugate gradient algorithm with a nonbonded cutoff of 8.0 Å. In stage one, the p38 protein and **39** were restrained such that the added TIP3P water molecules adjusted to their proper orientations. In stage two, the protein backbone was restrained such that the amino acid side chains were free to better accommodate **39**, which was particularly important for the manually formed p38β, p38δ, and p38γ systems. In stage three, the entire solvated system was minimized, without any restraint.

The MD simulations performed in this study followed a standard protocol consisting of gradual heating, density equilibration, equilibration, and production procedures in an isothermal isobaric ensemble (*NPT*, *P* = 1 atm and *T* = 300 K) MD. A minimized solvated system was used as the starting structure for subsequent MD simulations. In the 500 ps heating procedure, the system was gradually heated from 0 to 300 K in 50 ps, followed by density equilibration at 300 K for 500 ps, and then constant equilibration at 300 K for 500 ps. Following the equilibration procedure, each complex system underwent a 10 ns production procedure for conformation collection. The time step was set to 2 fs. A snapshot was taken every 10 ps to record the conformation trajectory during production MD. An 8 Å cutoff was applied to treat nonbonding interactions, such as short-range electrostatic and van der Waals interactions, whereas the particle-mesh-Ewald (PME) method was applied to treat long-range electrostatic interactions.[37] The SHAKE algorithm[38] was employed to constrain all bonds containing hydrogen atoms to their equilibrium lengths. We collected the trajectory in 50 ps intervals for the final 5 ns, covering 100 conformation snapshots for the structural and energetic analysis of each complex system.

Binding Free Energy Calculations. MM/GBSA[28] is a popular approach for investigating the energetic contribution of protein−small molecule binding affinities. The difference in binding free energy was computed for each molecular species including complexes, ligands, and proteins as follows:

$$\Delta G_{\text{binding}} = G_{\text{complex}} - [G_{\text{p38\#}} + G_{\text{compound 39}}]$$

where

$$G_{\text{molecule}} = \langle E_{\text{MM}}\rangle + \langle G_{\text{solvation}}^{\text{polar}}\rangle + \langle G_{\text{solvation}}^{\text{nonpolar}}\rangle - TS$$

$$\langle E_{\text{MM}}\rangle = \langle E_{\text{internal}}\rangle + \langle E_{\text{electrostatic}}\rangle + \langle E_{\text{vdW}}\rangle$$

and

$$G_{\text{solvation}}^{\text{nonpolar}} = \gamma A + \beta$$

$\langle ...\rangle$ denotes the average for a set of structures obtained from a series of snapshots along an MD trajectory. $\Delta G_{\text{binding}}$ is estimated from the contributions of gas-phase energies (i.e., $\langle E_{\text{MM}}\rangle$), solvation-free energies, including polar and nonpolar terms, and entropies. For the gas-phase energies, E_{internal} includes the bond, angle, and torsional energies, while $E_{\text{electrostatic}}$ and E_{vdW} represent electrostatic and van der Waals energies, respectively. The polar solvation, $G_{\text{solvation}}^{\text{polar}}$, is calculated using the generalized Born model.[28] The nonpolar solvation term, $G_{\text{solvation}}^{\text{nonpolar}}$, is calculated using constants of 0.00542 kcal mol⁻¹ Å⁻² for the surface-tension proportionality constant, γ, and 0.92 kcal mol⁻¹ for the nonpolar free energy of a point solute, β. The solvent-accessible surface area A varies for each molecule and is calculated by the program. The entropy term, TS, arises from changes in degrees of freedom, including the translational, rotational, and vibrational terms of the solute molecules and is estimated via the classical statistical thermodynamics approach. Configurational entropy was not included in the approach as it is computationally expensive with the normal mode method.

■ RESULTS AND DISCUSSION

Statistical Parameters of the CoMFA and CoMSIA Models. The statistical parameters of the CoMFA and CoMSIA models are summarized in Table 2. In the CoMFA column, an optimum number of principal components (ONC) = 3 was recommended based on an LOO cross-validated run with a q^2 value of 0.684; the subsequent nonvalidation R^2 value was 0.977, which was greater than the 0.6 criterion required for a good model. To further ensure the predictive ability of the CoMFA

Table 2. Statistical Results of the CoMFA and CoMSIA Models[a]

	CoMFA	CoMSIA
q^2	0.684	0.726
ONC	3	4
R^2	0.977	0.971
SEE	0.132	0.152
F	365.224	205.786
contributions		
steric	0.370	
electrostatic	0.630	0.636
HB acceptor		0.366

[a]Abbreviations used: (q^2) leave-one-out cross-validated (LOOCV) correlation coefficient; (ONC) optimum number of principal components; (R^2) non-cross-validated correlation coefficient; (SEE) standard error of the estimate; (HB) hydrogen bond.

models built from the training set, we conducted test set modeling by predicting the pIC_{50} values of test set compounds. Similar to the training set model, the constructed CoMSIA model was an acceptable model based on the obtained ONC of 4, LOO q^2 value of 0.726, and the subsequent nonvalidation R^2 value of 0.971. The CoMFA model contour map included 63% of the electrostatic field descriptor, but only 37% of the contributing steric field, indicating a greater influence of the electrostatic field. The electrostatic field descriptor in the CoMSIA model also contributed significantly to various combinations of the five molecular similarity indices. The CoMSIA model accounted for 63.6% of the electrostatic field and 36.6% of the H-bond acceptor field, and the highest cross-validated q^2 and satisfied R^2 values were subsequently chosen to provide drug-development guidelines.

The predicted pIC_{50} values generated from the CoMFA and CoMSIA models are listed in Table S1 of the Supporting Information. This table also includes the experimentally observed pIC_{50} values and the residuals defined as the experimentally observed pIC_{50} values minus the model-predicted pIC_{50} values. The experimentally observed pIC_{50} values are plotted versus the modeled pIC_{50} values in Figure 3. The CoMFA and CoMSIA models indicated that the residuals between the predicted and experimentally observed pIC_{50} training set values ranged from +0.206 (compound **38** in the CoMSIA model) to −0.373 (compound **3** in the CoMSIA model).

CoMFA Model Interpretation. Figure 4 provides the steric and electrostatic contour maps obtained via CoMFA modeling. In the steric field shown in Figure 4A, the yellow contour on R_5 of the pyrazole moiety suggests that a bulky group, such as a methyl group in compound **3** ($IC_{50} > 100$ μM), is responsible for a reduction of the inhibitory activity. The green contour on the left suggests that a benzoyl moiety modification improves the inhibitory activity, whereas the outer yellow contour restricts the size of the modification agent. A comparison between the electrostatic fields generated by the CoMFA (Figure 4B) and CoMSIA (Figure 5B) models is provided in the CoMSIA section.

Interpretation of the CoMSIA Model. The CoMSIA results are presented in Figure 5. Figure 5A is a contour map of H-bond acceptor preferences. The two purple contours suggest that the H-bond acceptors around the two hydroxyl groups on the X-substituent of **39** are important for its inhibitory activity. The red contour on the amine group of **39** indicates that the H-bond acceptors are unfavorable. This inference is supported by the increased IC_{50} values observed for compounds **2** (a cyanide therein) and **3** (a hydroxyl therein).
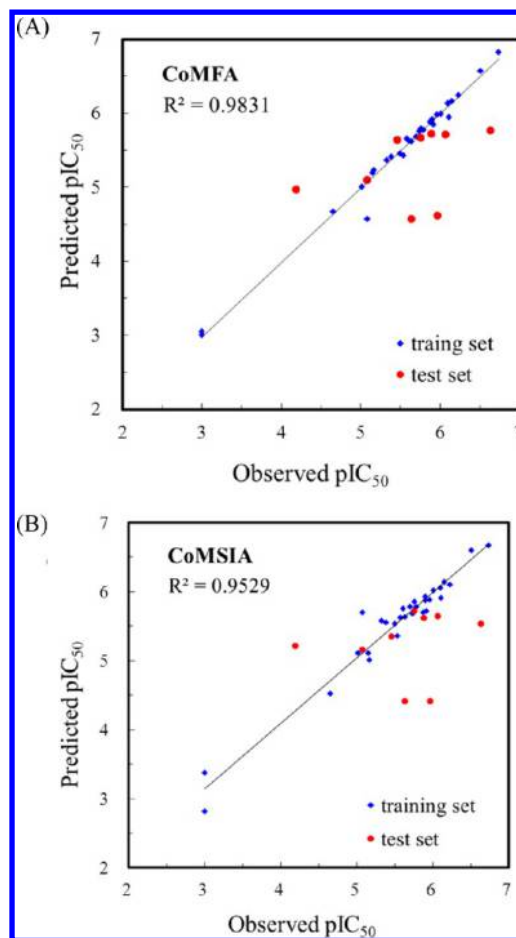
Figure 3. CoMFA (A) and CoMSIA (B) predictions for the training (blue square dots) and test (red circle dots) sets regarding inhibitory activities against p38α kinase. The solid line is the regression line for the training set predictions.

The two electrostatic fields generated by CoMFA and CoMSIA (Figures 4B and 5B) are in agreement and share a common feature: that the electronegative groups attached to the N-phenyl ring (highlighted by red contours in Figures 4B and 5B) are important for the resultant inhibitory activity through reducing the N-phenyl ring's electron density (suggested as a blue contour therein, Figure 5B). An electron-withdrawing group at the para (i.e., R_2 in Table 1) or ortho (i.e., R in Table 1) position relative to the pyrazole group linkage possesses an induction ability allowing it to dissipate the π electron density on the N-phenyl ring. Consequently, compounds 6, 7, and 8, which possess a fluoro atom at the para, meta, or ortho site (R_2, R_1, and R in Table 1) relative to pyrazole, respectively, exhibit inhibitory activities of 1.1, 6.7, and 2.86 μM.

Meanwhile, the electropositive preference suggested by the blue contour on R_3 in Figure 5B is in accord with the H-bond acceptor disfavoring property indicated by the red contour on R_3 in Figure 5A. We believe that these two contours account for the least potent compounds, **2** and **3**, which possess a cyanide or hydroxyl group, respectively, while the remaining compounds in our training set possess an amine group.

In the test set predictions, both the CoMFA and CoMSIA models significantly underestimated the pIC_{50} values of compounds **1**, **4**, and **34** but greatly overestimated the pIC_{50} value of compound **5**. Otherwise, the inhibitory activities of the other six compounds in test set were fairly accurate. The underestimated
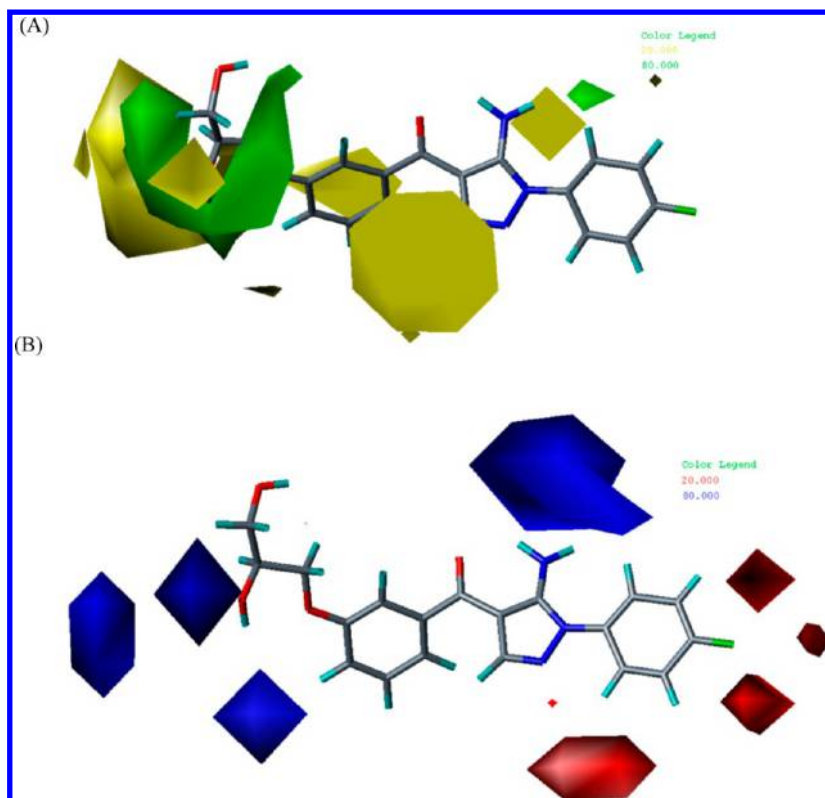
Figure 4. Standard coefficient contour maps obtained from CoMFA analysis of compound **39**. (A) Steric fields: green contours indicate regions where bulky groups enhance activity, whereas yellow contours indicate regions where bulky groups decrease activity. (B) Electrostatic fields: blue contours represent regions where electron-donating groups increase activity, whereas red contours represent regions where electron-withdrawing groups increase activity.
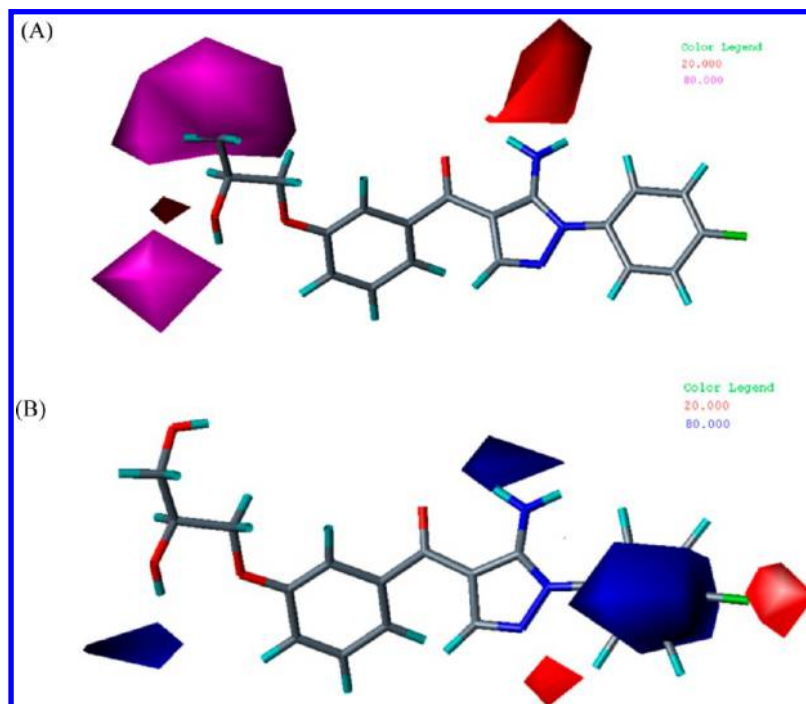
Figure 5. Standard coefficient contour maps from CoMSIA analysis of compound **39**. (A) H-bond acceptor fields: purple contours represent regions that prefer H-bond acceptors, whereas the red contour represents a region that disfavors hydrogen bond acceptors. (B) Electrostatic fields: blue contours represent regions where electron-donating groups increase activity, whereas red contours represent regions where electron-withdrawing groups increase activity.

pIC_{50} obtained for compound **34** could be attributed to the long 2-(1-hydroxycyclopentyl)ethyl chain orienting in a way to be in proximity to the sterically disfavored yellow contour, instead of being in the sterically favored green contour, in the CoMFA steric field (Figure 4A). As seen for compound **4**, which possesses a methyl group at the R-site, the penalty is attributed to the methyl group, which serves as an electron-donating group, in violation of the electrostatic fields shown in Figure 4B and 5B, rather than a hydrogen

or fluorine atom, as observed in the other training and test set compounds. Compounds **4** (experimentally observed pIC$_{50}$ = 1.08 μM, R = CH$_3$) and **8** (experimentally observed pIC$_{50}$ = 2.86 μM, R = F) are similar, with the exception of the substituents found at R. It is possible that van der Waals interaction occurs between the methyl group of **4** and p38α, but the models constructed here do not include this field; therefore, the inhibitory activity of **4** was underestimated.

Molecular Dynamics Simulations of Compound 39-Bound p38 MAPK Systems. In addition to the structure-activity analysis, MD simulations were performed for 10 ns to investigate the mode of **39** binding to the four p38 MAPK isoforms. To explore the dynamic stability of the complexes and ensure rationality of the sampling method, we monitored the root-mean-square deviation (RMSD) from the starting structure, as shown in Figure S1. The plots demonstrate that the RMSD of each system reaches a converged stage after 4 ns, indicating that the systems are stable and equilibrated and that conducting conformation sampling between 6 and 10 ns is reliable.

In the following, we compare our MD results to the p38α-**39** structure determined via X-ray crystallography (PDB code: 2GFS) and correlate several interactions to our QSAR models. Figure 6A depicts the two superimposed p38α-**39** structures.
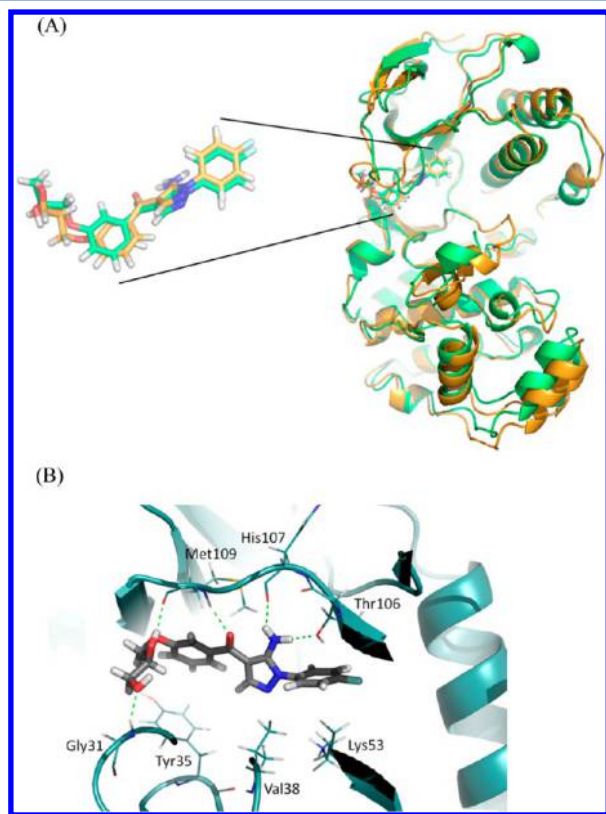

Figure 6. Binding mode of **39** within the p38α MAPK ATP-binding site. (A) A comparison of binding modes retrieved from a protein data bank (in lime green) and from an average structure from our MD analyses (in beige). (B) An enhanced view of the binding mode determined via MD analysis.

The MD-generated structure (shown in beige) represents an average structure obtained from the trajectory observed in the second half of the 10 ns simulation. Because some fragments are missing from the X-ray structure (shown in lime green in Figure 6A), we estimated the RMSD for **39** alone, instead of the entire complex. The RMSD calculated for **39** is 1.21 Å when considering the

heavy atoms and 1.60 Å when considering all atoms. Figure 6B presents the detailed binding interaction of **39** with the ATP site of p38α MAPK concluded from our MD results and in agreement with the X-ray structure. The major H-bond interactions occur in the two amino hydrogen atoms in **39** linking to the hydroxyl oxygen atom in the Thr106 side chain and the carbonyl oxygen atom in the His107 backbone, showing hydrogen-bond occupancies of 95% and 98%, respectively (Supporting Information Figure S2) and with separation distances 1.75 and 2.27 Å in the X-ray structure. This finding is in accord with the red contour in Figure 5A, indicating that the H-bond acceptor in the amine group of **39** is not favored. The blue contour on the N-phenyl ring shown in Figure 5B is related to the H-bond with Thr106 because the smaller electronegative property of the N-phenyl ring allows the oxygen atom on Thr106 to orient properly as it approaches its H-bond partner. Both our MD result and the X-ray structure show the **39** N-phenyl ring interacts with a basic residue, Lys53, through both cation-π and aliphatic-π interactions. In the X-ray structure, the distance between the positive charge in the end of Lys53 residue and the center of mass of the N-phenyl ring is 4.74 Å (such a cation-π interaction is in 91% occupancy percentage in our entire MD trajectory), and the center of mass of the Lys53 long chain and the center of mass of the N-phenyl ring is 4.56 Å. Some minor interactions are found as follows. The **39** benzoyl ring moiety interacts with the Tyr35 ring via a π-π interaction, with an observed separation distance ranging from 4.3 to 5.3 Å in the 10 ns MD simulation, in accord to 4.74 Å in the X-ray structure. In addition, there are three H-bonds in lower occupancy percentages: the **39** carbonyl oxygen atom and two hydroxyl oxygen atoms link to the Met109 amino hydrogen atom, the Met109 carbonyl oxygen atom, and the Gly31 amino hydrogen atom, with their separation distances 1.71, 3.19, and 4.54 Å found in X-ray structure, and with 80%, 21%, and 37% occupancy percentages in our MD results. The binding pocket is primarily hydrophobic with the exception of the Lys53. The hydrophobicity of the binding pocket is also suggested by the MM/GBSA calculation (Table 3), where the absolute value of the ΔG_{vdW} term (−47.97 kcal/mol) is greater than that of the ΔG_{ele} term (−31.82 kcal/mol).

To compare the different binding modes of **39** to the four p38 MAPK isoforms with the in vitro selectivity profile of 105 kinases, showing that **39** only inhibit p38α and p38β and not p38γ and p38δ,[20] we also performed MD simulations on the p38β-**39**, p38γ-**39**, and p38δ-**39** complex systems. The MD-simulated binding modes of p38β_{DFG-in}-**39** and p38$\beta_{DFG-out}$-**39** are shown in Figure 7A and B. Similar to the p38α−**39** complex, in the p38β-**39** complex, compound **39** is secured by Lys53, Thr106, Thr107, and Met109. More specifically, cation-π and aliphatic-π interactions occur between Lys53 and the N-phenyl ring of **39**. The two amino hydrogen atoms on **39** are anchored by the side chain hydroxyl oxygen atom of Thr106 and the backbone carbonyl oxygen atom of Thr107 (His107 in p38α). The backbone amino nitrogen and carbonyl oxygen atoms of Met109 form H-bonds with the compound **39** carbonyl oxygen atom and an adjacent hydroxyl hydrogen atom. In addition, Ser40 is minimally predicted (11% and 28% in p38β_{DFG-in}−**39** and p38$\beta_{DFG-out}$-**39**, respectively) to undergo H-bond formation with a remote hydroxyl group in **39**. This hydroxyl group is occasionally H-bonded to the p38α Gly31 backbone (37% occupancy). The percentages of H-bond occupancy for p38β_{DFG-in}-**39** and p38β_{DFG-in}-**39** are provided in Supporting Information Figures S3 and S4, respectively. The average numbers of H-bonds are 3.95 and 4.14 for p38β_{DFG-in}-**39** and

Table 3. Binding Free Energies Calculated via MM/GBSA for the Binding of Compound 39 to p38 MAPKs[a]

	ΔG_{vdw}	ΔG_{ele}	$\Delta G_{polar,sol}$	$\Delta G_{nonpol,sol}$	ΔG_{MM}	ΔG_{sol}	ΔG_{bind}	predicted IC$_{50}$
p38α Δ (DFG-in)	−47.97	−31.82	43.31	−6.43	−79.79	36.88	−42.92	0.7[b]
p38β Δ (DFG-out)	−44.94	−35.06	44.59	−6.14	−80.00	38.45	−41.54	3.6
p38β Δ (DFG-in)	−46.63	−29.70	40.13	−5.92	−76.33	34.21	−42.12	1.37
p38γ Δ (DFG-in)	−42.80	−26.00	39.50	−5.30	−68.80	34.20	−34.60	4.4×10^5
p38δ Δ (DFG-in)	−35.74	0.99	19.45	−4.11	−34.74	15.34	−19.40	6.2×10^{16}

[a]All energies are reported as kilocalories per mole, and IC$_{50}$ values are in micromolar. [b]The IC$_{50}$ for p38α was obtained experimentally.[20]
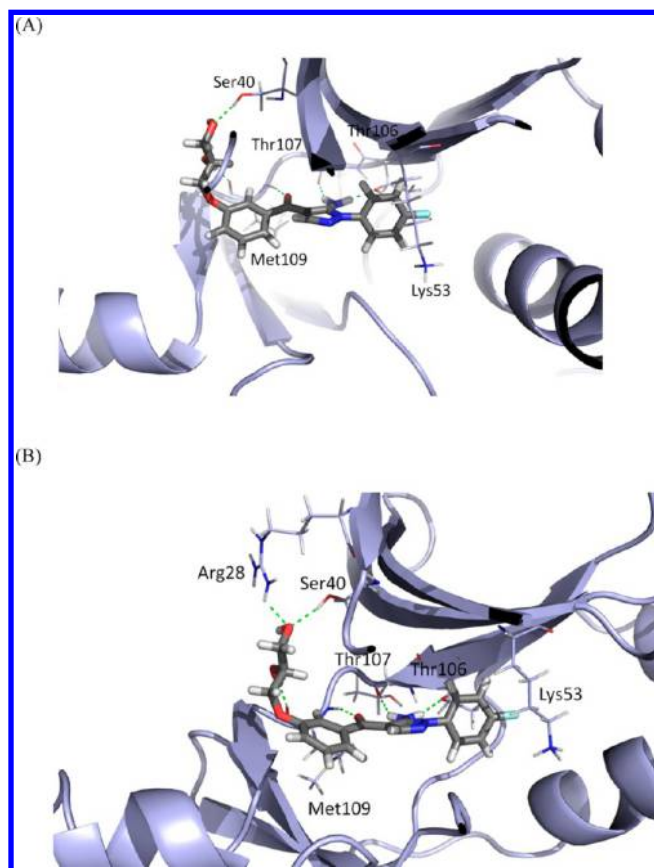

Figure 7. Enhanced views of the binding mode determined via MD analysis. (A) **39** bound to p38$\beta_{DGF\text{-}in}$. (B) **39** bound to p38$\beta_{DGF\text{-}out}$.

Figure 8. Enhanced view of **39** bound to p38γ, as determined via MD analysis.

Figure 9. Enhanced view of **39** bound to p38δ, as determined via MD analysis.

p38$\beta_{DFG\text{-}out}$-**39**, respectively, in accord with the MM/GBSA data, which indicates ΔG_{ele} values of −29.70 and −35.06 kcal/mol for p38$\beta_{DFG\text{-}in}$-**39** and p38$\beta_{DFG\text{-}out}$-**39**, respectively. The overall ΔG_{bind} values are similar (−42.12 kcal/mol for p38$\beta_{DFG\text{-}in}$-**39** and −41.54 kcal/mol for p38$\beta_{DFG\text{-}out}$-**39**) but show a slight preference for the DFG-in conformation, in accord with the fact that the studied compound series is classified to DFG-in binding mode.

As shown in Figure 8, the MD-simulated p38γ-**39** complex displays fewer H-bonding interactions compared to the p38α and p38β MAPK complexes. The amino hydrogen atom and the carbonyl oxygen atom of **39** are secured by Pro110 and Met112, with 92% and 97% H-bond occupancies, respectively (Supporting Information Figure S5). The positively charged terminus of the Lys56 side chain (which is equivalent to Lys53 in p38α and p38β MAPK) is approximately 5.6 Å from the N-phenyl ring and provides marginal cation-π interactions, but its aliphatic hydrocarbon chain is not properly oriented to provide aliphatic-π interactions when compared with the p38α and p38β MAPK systems. MM/GBSA predicts the $\Delta G_{binding}$ value to be approximately
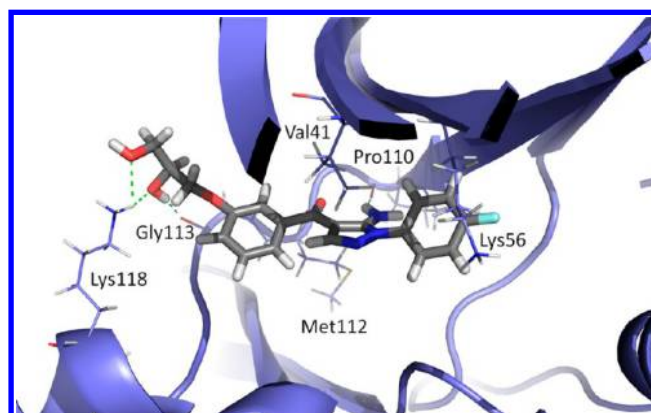
8 kcal/mol less than the values predicted for the p38α and p38β MAPK systems.

Figure 9 presents the mode of **39** binding to p38δ MAPK. In this model, H-bonding is barely maintained by Gln111 (36% occupancy, Supporting Information Figure S6), in accord with the ΔG_{ele} value of +0.99 kcal/mol, as shown in Table 3. Sigma-π interactions were noted at the Thr112-benzoyl ring, Val31-benzoyl ring, and Leu167-N-phenyl ring exhibiting 33%, 25%, and 8% occupancies, respectively, for the entire MD duration (Supporting Information Figure S5B). When the Discovery Studio 3.5 LigFit module[39] was employed to estimate the pocket volume, the p38δ MAPK pocket volume was found to be the greatest among the studied complexes (451, 660, 552, 522, and 743 Å^3 for p38α, p38$\beta_{DFG\text{-}in}$, p38$\beta_{DFG\text{-}out}$, p38γ, and p38δ). These data explain the smallest value ΔG_{vdW} of −35.74 kcal/mol

Figure 10. Comparison of the position of Tyr35 of p38α MAPK: (A) among different p38 MAPK isoforms bound to **39**, where the color codes for α, β, γ, and δ are teal, light blue, blue, and purple, respectively; and (B) between apo p38α and **39**-bound p38α, where the color codes for the secondary structures are gray, green, red, and cyan for coils, turns, helices, and β strands, respectively.
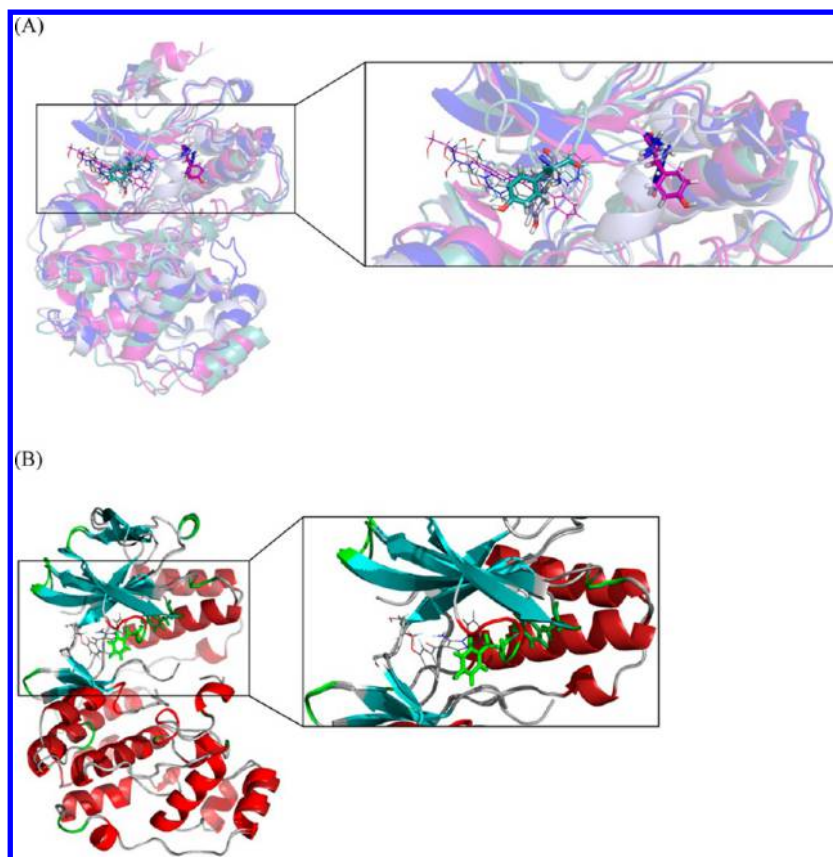
in Table 3, as the hydrophobic amino acid residues are too far away to contact **39**.

We also predicted IC$_{50}$ values based on an approximation of $\Delta G_{binding} \approx RT \ln IC_{50}$.[40] Using the p38α-**39** IC$_{50}$ value of 0.7 μM as a reference, $\Delta\Delta G_{binding} = \Delta G_{binding,a} - \Delta G_{binding,b} \approx RT \ln(IC_{50,a}/IC_{50,b})$. The predicted IC$_{50}$ values for p38γ and p38δ in Table 3 suggest that compound **39** cannot bind to these two kinases given that the predicted IC$_{50}$ values for p38α and p38β are at the micromolar level. This finding is in accord with the kinase selectivity profile indicating that compound **39** inhibits p38α and p38β, but not p38γ and p38δ.[20]

The Tyr35 residue in p38α exhibits π-π interactions with the benzoyl ring and is conserved among the four p38 MAPK isoforms (Tyr35 in p38β, Tyr36 in p38γ, and Tyr38 in p38δ). It is located in a coil (possibly from Val30 to Gly36) linking the β3 strand (Tyr24 to Pro29) to the β4 strand (Gly36 or Ser37 to Asp43) in the N-lobe of the kinase domain. In Goldstein's p38α-**39** X-ray crystallography structure,[20] the secondary structure in the center of Tyr35 differs dramatically from other p38α structures for apo or small molecule-bound forms and other p38 MAPK isoform structures maintained in this fashion. The superimposition of the four p38 MAPK-**39** complexes shown in Figure 10A reveals that Tyr35 in p38α points toward the bound inhibitor, whereas the equivalent Tyr residues in the other p38 MAPK isoforms point toward a helix linking the β4 and β5 strands within the N-lobe. Figure 10B provides a comparison of apo p38α (PDB code: 1R39[41]) with **39**-bound p38α. The linkage between the β3 and β4 strands in the **39**-bound p38α structure (extracted from PDB: 2GFS[20]) is found in the secondary structure of the coil-helix-turn-coil (determined by

Discovery Studio 3.5[39]), placing Tyr35 in the turn region. The short helix results in less expansion of the linkage and confers π−π interactions between Tyr35 and the inhibitor. If such a structural deformation were to also occur in the p38β−**39** complex, the increased negative ΔG_{vdW} term for **39**-bound p38β could lead to an absolute $\Delta G_{bind, p38β}$ value that is greater than the absolute $\Delta G_{bind, p38α}$ value, thereby potentially explaining the dissociation constants, $K_d = 0.20$ for p38α and $K_d = 0.05$ for p38β, observed in kinase assays by Goldstein et al.[20] Our binding pocket calculations for p38α and p38β in their DFG-in conformations provided values of 451 and 552 Å^3, respectively. Therefore, inhibitors developed in the future should be modified to fit in the p38α pocket in a compact fashion to discriminate p38β.

■ CONCLUSION

We performed 3D-QSAR analysis on a series of p38α MAPK inhibitors based on a 4-benzoyl-5-aminopyzrazole core. In addition, we conducted MD simulations and MM/GBSA analysis of **39** bound to the four p38 isoforms to highlight its structural preferences for p38δ and p38γ MAPK. The MD simulation results for p38α-**39**, which are in accord with the X-ray crystallographic data generated by Goldstein et al.,[20] show that **39** uses two hydrogen atoms in the amino group as hydrogen-bond donors and a carbonyl oxygen atom and two hydroxyl oxygen atoms in the diol group as hydrogen-bond acceptors in interactions with Thr106, His107, Met109, and Gly31 of p38α. Lys53 exhibits cation-π and aliphatic-π interactions with the inhibitor's N-phenyl ring. Additional van der Waals interactions are observed between the benzoyl ring and the aromatic Tyr35 residue. Both the CoMFA and CoMSIA models also agree with the

highlights of the MD simulations. These computationally obtained results will aid in the rational design of novel p38α MAPK inhibitors.

ASSOCIATED CONTENT

S Supporting Information

Figures S1-S6 and Table S1 as mentioned in the text. This material is available free of charge via the Internet at http://pubs.acs.org.

AUTHOR INFORMATION

Corresponding Author

*E-mail: cnyang@nuk.edu.tw.

Notes

The authors declare no competing financial interest.

ACKNOWLEDGMENTS

REFERENCES

(1) Lee, J. C.; Laydon, J. T.; McDonnell, P. C.; Gallagher, T. F.; Kumar, S.; Green, D.; McNulty, D.; Blumenthal, M. J.; Heys, J. R.; Landvatter, S. W.; et al. A protein kinase involved in the regulation of inflammatory cytokine biosynthesis. *Nature* **1994**, *372*, 739−46.

(2) Jiang, Y.; Chen, C.; Li, Z.; Guo, W.; Gegner, J. A.; Lin, S.; Han, J. Characterization of the structure and function of a new mitogen-activated protein kinase (p38beta). *J. Biol. Chem.* **1996**, *271*, 17920−6.

(3) Li, Z.; Jiang, Y.; Ulevitch, R. J.; Han, J. The primary structure of p38 gamma: a new member of p38 group of MAP kinases. *Biochem. Biophys. Res. Commun.* **1996**, *228*, 334−40.

(4) Jiang, Y.; Gram, H.; Zhao, M.; New, L.; Gu, J.; Feng, L.; Di Padova, F.; Ulevitch, R. J.; Han, J. Characterization of the structure and function of the fourth member of p38 group mitogen-activated protein kinases, p38delta. *J. Biol. Chem.* **1997**, *272*, 30122−8.

(5) Zayzafoon, M.; Botolin, S.; McCabe, L. R. P38 and activating transcription factor-2 involvement in osteoblast osmotic response to elevated extracellular glucose. *J. Biol. Chem.* **2002**, *277*, 37212−8.

(6) Goh, K. C.; Haque, S. J.; Williams, B. R. p38 MAP kinase is required for STAT1 serine phosphorylation and transcriptional activation induced by interferons. *EMBO J.* **1999**, *18*, 5601−8.

(7) Freshney, N. W.; Rawlinson, L.; Guesdon, F.; Jones, E.; Cowley, S.; Hsuan, J.; Saklatvala, J. Interleukin-1 activates a novel protein kinase cascade that results in the phosphorylation of Hsp27. *Cell* **1994**, *78*, 1039−49.

(8) Shiryaev, A.; Moens, U. Mitogen-activated protein kinase p38 and MK2, MK3 and MK5: menage a trois or menage a quatre? *Cell Signal* **2010**, *22*, 1185−92.

(9) Goedert, M.; Cuenda, A.; Craxton, M.; Jakes, R.; Cohen, P. Activation of the novel stress-activated protein kinase SAPK4 by cytokines and cellular stresses is mediated by SKK3 (MKK6); comparison of its substrate specificity with that of other SAP kinases. *EMBO J.* **1997**, *16*, 3563−71.

(10) Cuenda, A.; Cohen, P.; Buee-Scherrer, V.; Goedert, M. Activation of stress-activated protein kinase-3 (SAPK3) by cytokines and cellular stresses is mediated via SAPKK3 (MKK6); comparison of the specificities of SAPK3 and SAPK2 (RK/p38). *EMBO J.* **1997**, *16*, 295−305.

(11) Cuenda, A.; Rousseau, S. p38 MAP-kinases pathway regulation, function and role in human diseases. *Biochim. Biophys. Acta* **2007**, *1773*, 1358−75.

(12) Ambrosino, C.; Nebreda, A. R. Cell cycle regulation by p38 MAP kinases. *Biol Cell* **2001**, *93*, 47−51.

(13) Bulavin, D. V.; Tararova, N. D.; Aksenov, N. D.; Pospelov, V. A.; Pospelova, T. V. Deregulation of p53/p21Cip1/Waf1 pathway

contributes to polyploidy and apoptosis of E1A+cHa-ras transformed cells after gamma-irradiation. *Oncogene* **1999**, *18*, 5611−9.

(14) Herlaar, E.; Brown, Z. p38 MAPK signalling cascades in inflammatory disease. *Mol Med Today* **1999**, *5*, 439−47.

(15) Tibbles, L. A.; Woodgett, J. R. The stress-activated protein kinase pathways. *Cell. Mol. Life Sci.* **1999**, *55*, 1230−54.

(16) Clark, A. R.; Dean, J. L. The p38 MAPK Pathway in Rheumatoid Arthritis: A Sideways Look. *Open Rheumatol. J.* **2012**, *6*, 209−219.

(17) Rutgeerts, P.; D'Haens, G.; Targan, S.; Vasiliauskas, E.; Hanauer, S. B.; Present, D. H.; Mayer, L.; Van Hogezand, R. A.; Braakman, T.; DeWoody, K. L.; Schaible, T. F.; Van Deventer, S. J. Efficacy and safety of retreatment with anti-tumor necrosis factor antibody (infliximab) to maintain remission in Crohn's disease. *Gastroenterology* **1999**, *117*, 761−9.

(18) Chung, K. F. p38 mitogen-activated protein kinase pathways in asthma and COPD. *Chest* **2011**, *139*, 1470−9.

(19) Swapna, D.; Prathyusha Pooja, V.; Sucharitha, D.; Sunitha, K.; Swetha, M. A review of p38 kinase inhibitors as anti-inflammatory drug targets. *Int. J. Pharm. Technol.* **2010**, *2*, 16.

(20) Goldstein, D. M.; Alfredson, T.; Bertrand, J.; Browner, M. F.; Clifford, K.; Dalrymple, S. A.; Dunn, J.; Freire-Moar, J.; Harris, S.; Labadie, S. S.; La Fargue, J.; Lapierre, J. M.; Larrabee, S.; Li, F.; Papp, E.; McWeeney, D.; Ramesha, C.; Roberts, R.; Rotstein, D.; San Pablo, B.; Sjogren, E. B.; So, O. Y.; Talamas, F. X.; Tao, W.; Trejo, A.; Villasenor, A.; Welch, M.; Welch, T.; Weller, P.; Whiteley, P. E.; Young, K.; Zipfel, S. Discovery of S-[5-amino-1-(4-fluorophenyl)-1H-pyrazol-4-yl]-[3-(2,3-dihydroxypropoxy)phenyl]me thanone (RO3201195), an orally bioavailable and highly selective inhibitor of p38 MAP kinase. *J. Med. Chem.* **2006**, *49*, 1562−75.

(21) Li, D.; Liu, M. S.; Ji, B.; Hwang, K.; Huang, Y. Coarse-grained molecular dynamics of ligands binding into protein: The case of HIV-1 protease inhibitors. *J. Chem. Phys.* **2009**, *130*, 215102.

(22) Estacio, S. G.; Moreira, R.; Guedes, R. C. Characterizing the dynamics and ligand-specific interactions in the human leukocyte elastase through molecular dynamics simulations. *J. Chem. Inf. Model.* **2011**, *51*, 1690−702.

(23) Shenoy, R. T.; Chowdhury, S. F.; Kumar, S.; Joseph, L.; Purisima, E. O.; Sivaraman, J. A combined crystallographic and molecular dynamics study of cathepsin L retrobinding inhibitors. *J. Med. Chem.* **2009**, *52*, 6335−46.

(24) Karkola, S.; Lilienkampf, A.; Wahala, K. A 3D QSAR model of 17beta-HSD1 inhibitors based on a thieno[2,3-d]pyrimidin-4(3H)-one core applying molecular dynamics simulations and ligand-protein docking. *ChemMedChem* **2008**, *3*, 461−72.

(25) Yang, Y.; Shen, Y.; Liu, H.; Yao, X. Molecular dynamics simulation and free energy calculation studies of the binding mechanism of allosteric inhibitors with p38alpha MAP kinase. *J. Chem. Inf. Model.* **2011**, *51*, 3235−46.

(26) Cramer, R. D.; Patterson, D. E.; Bunce, J. D. Comparative molecular field analysis (CoMFA). 1. Effect of shape on binding of steroids to carrier proteins. *J. Am. Chem. Soc.* **1988**, *110*, 5959−67.

(27) Klebe, G.; Abraham, U.; Mietzner, T. Molecular similarity indices in a comparative analysis (CoMSIA) of drug molecules to correlate and predict their biological activity. *J. Med. Chem.* **1994**, *37*, 4130−46.

(28) Onufriev, A.; Bashford, D.; Case, D. A. Exploring protein native states and large-scale conformational changes with a modified generalized born model. *Proteins* **2004**, *55*, 383−94.

(29) *Sybyl*, 8.1; Tripos International: St. Louis.

(30) Case, D. A.; Darden, T. A.; Cheatham, I., T.E.; Simmerling, C. L.; Wang, J.; Duke, R. E.; Luo, R.; Walker, R. C.; Zhang, W.; Merz, K. M.; Roberts, B.; Wang, B.; Hayik, S.; Roitberg, A.; Seabra, G.; Kolossváry, I.; Wong, K. F.; Paesani, F.; Vanicek, J.; Liu, J.; Wu, X.; Brozell, S. R.; Steinbrecher, T.; Gohlke, H.; Cai, Q.; Ye, X.; Wang, J.; Hsieh, M.-J.; Cui, G.; Roe, D. R.; Mathews, D. H.; Seetin, M. G.; Sagui, C.; Babin, V.; Luchko, T.; Gusarov, S.; Kovalenko, A.; Kollman, P. A. *AMBER*, 11; University of California: San Francisco, 2010.

(31) Duan, Y.; Wu, C.; Chowdhury, S.; Lee, M. C.; Xiong, G.; Zhang, W.; Yang, R.; Cieplak, P.; Luo, R.; Lee, T.; Caldwell, J.; Wang, J.; Kollman, P. A point-charge force field for molecular mechanics

simulations of proteins based on condensed-phase quantum mechanical calculations. *J. Comput. Chem.* **2003**, *24*, 1999−2012.

(32) Hornak, V.; Abel, R.; Okur, A.; Strockbine, B.; Roitberg, A.; Simmerling, C. Comparison of multiple Amber force fields and development of improved protein backbone parameters. *Proteins* **2006**, *65*, 712−25.

(33) Badrinarayan, P.; Sastry, G. N. Sequence, structure, and active site analyses of p38 MAP kinase: exploiting DFG-out conformation as a strategy to design new type II leads. *J. Chem. Inf. Model.* **2011**, *51*, 115−29.

(34) Wang, J.; Wang, W.; Kollman, P. A.; Case, D. A. Automatic atom type and bond type perception in molecular mechanical calculations. *J. Mol. Graph. Model.* **2006**, *25*, 247−60.

(35) Jakalian, A.; Jack, D. B.; Bayly, C. I. Fast, efficient generation of high-quality atomic charges. AM1-BCC model: II. Parameterization and validation. *J. Comput. Chem.* **2002**, *23*, 1623−41.

(36) Jorgensen, W. L.; Chandrasekhar, J.; Madura, J. D.; Impey, R. W.; Klein, M. L. Comparison of simple potential functions for simulating liquid water. *J. Chem. Phys.* **1983**, *79*, 10.

(37) Darden, T.; York, D.; Pedersen, L. Particle mesh Ewald: An N·log(N) method for Ewald sums in large systems. *J. Chem. Phys.* **1993**, *98*, 10089.

(38) Ryckaert, J.-P.; Ciccotti, G.; Berendsen, H. Numerical Integration of the Cartesian Equations of Motion of a System with Constraints: Molecular Dynamics of *n*-Alkanes. *J. Comput. Phys.* **1977**, *23*, 15.

(39) *Discovery Studio Modeling Environment*, Accelrys Software Inc.: San Diego, 2012.

(40) Wang, J.; Morin, P.; Wang, W.; Kollman, P. A. Use of MM-PBSA in reproducing the binding free energies to HIV-1 RT of TIBO derivatives and predicting the binding mode to HIV-1 RT of efavirenz by docking and MM-PBSA. *J. Am. Chem. Soc.* **2001**, *123*, 5221−30.

(41) Patel, S. B.; Cameron, P. M.; Frantz-Wattley, B.; O'Neill, E.; Becker, J. W.; Scapin, G. Lattice stabilization and enhanced diffraction in human p38 alpha crystals by protein engineering. *Biochim. Biophys. Acta* **2004**, *1696*, 67−73.